HHS Public Access

Author manuscript

Biol Psychiatry. Author manuscript; available in PMC 2021 August 01.

Published in final edited form as:

Biol Psychiatry. 2020 August 01; 88(3): 215–223. doi:10.1016/j.biopsych.2020.01.004.

Aberrant Cortical Ensembles and Schizophrenialike Sensory Phenotypes in *Setd1a*$^{+/-}$ Mice

Jordan P. Hamm,
Neurotechnology Center, Columbia University, New York, New York

Neuroscience Institute, Georgia State University, Atlanta, Georgia

Yuriy Shymkiv,
Neurotechnology Center, Columbia University, New York, New York

Jun Mukai,
College of Physicians and Surgeons; Mortimer B. Zuckerman Mind Brain and Behavior Institute, Columbia University, New York, New York

Laboratory of Molecular Psychiatry and Neuroscience, Research and Development Center for Precision Medicine, University of Tsukuba, Tsukuba, Ibaraki, Japan

Joseph A. Gogos,
Department of Biological Sciences; Department of Physiology and Cellular Biophysics, Columbia University, New York, New York

College of Physicians and Surgeons; Mortimer B. Zuckerman Mind Brain and Behavior Institute, Columbia University, New York, New York

Department of Neuroscience, Columbia University, New York, New York

Rafael Yuste
Neurotechnology Center, Columbia University, New York, New York

Abstract

BACKGROUND—A breakdown of synchrony within neuronal ensembles leading to destabilization of network "attractors" could be a defining aspect of neuropsychiatric diseases such as schizophrenia, representing a common downstream convergence point for the diverse etiological pathways associated with the disease. Using a mouse genetic model, we demonstrated that altered ensembles are associated with pathological sensory cortical processing phenotypes resulting from loss of function mutations in the *Setd1a* gene, a recently identified rare risk genotype with very high penetrance for schizophrenia.

METHODS—We used fast 2-photon calcium imaging of neuronal populations (calcium indicator GCaMP6s, 10 Hz, 100–250 cells, layer 2/3 of primary visual cortex, i.e., V1) in awake head-fixed

Address correspondence to Jordan Hamm, Ph.D., Neuroscience Institute, Georgia State University, 813 Petit Science Center, 100 Piedmont Ave., Atlanta, GA 30303; hamm.jordan@gmail.com.

The authors report no biomedical financial interests or potential conflicts of interest.

Supplementary material cited in this article is available online at https://doi.org/10.1016/j.biopsych.2020.01.004.

mice (*Setd1a*$^{+/-}$ vs. wild-type littermate control) during rest and visual stimulation with moving full-field square-wave gratings (0.04 cycles per degree, 2.0 cycles per second, 100% contrast, 12 directions). Multielectrode recordings were analyzed in the time-frequency domain to assess stimulus-induced oscillations and cross-layer phase synchrony.

RESULTS—Neuronal activity and orientation/direction selectivity were unaffected in *Setd1a*$^{+/-}$ mice, but correlations between cell pairs in V1 showed altered distributions compared with wild-type mice, in both ongoing and visually evoked activity. Furthermore, population-wide "ensemble activations" in *Setd1a*$^{+/-}$ mice were markedly less reliable over time during rest and visual stimulation, resulting in unstable encoding of basic visual information. This alteration of ensembles coincided with reductions in alpha and high-gamma band phase synchrony within and between cortical layers.

CONCLUSIONS—These results provide new evidence for an ensemble hypothesis of schizophrenia and highlight the utility of *Setd1a*$^{+/-}$ mice for modeling sensory-processing phenotypes.

Keywords

Attractor; Cortex; Oscillation; *Setd1a*; Two-photon; Visual

Altered cortical processing of sensory stimuli is a highly consistent finding in individuals with schizophrenia (SZ) (1–3). While significant focus has been dedicated to investigating prefrontal cortex (PFC) and dopaminergic systems in SZ, many cellular and molecular aberrations in the disease affect all cortical regions (4,5), suggesting that basic investigations of the sensory cortex could be a valid strategy for linking disease-relevant alterations in molecular, cellular, and circuit function. Moreover, areas such as the primary visual cortex (V1) are well characterized structurally and functionally and are highly translatable, e.g., to rodent models (6–8).

The growing need for such a translational inroad to studying SZ has been made evident by accumulating evidence that SZ likely lacks a singular genetic cause across cases (9). Still, the diagnosis of SZ may nevertheless have a biological signature that is common across cases and represents the downstream intersection points of these myriad genetic causes. One candidate for this common pathophysiology lies not at the molecular or cellular level, but at the "ensemble" (i.e., neuronal group) level (10), where distributions of recurrent synaptic connections among local groups of neurons first form stable emergent activity patterns that repeat over time, forming computational building blocks of the cortex (11), similar to "attractors" in a neural network (12). Such a "degraded attractor" hypothesis of SZ has considerable explanatory power and utility, because it not only provides a logical common pathophysiological intersection point, but also forms an intuitive basis for linking biology to phenomenology. Pathologically variable activation patterns due to weak attractors in neuronal circuits cortex wide (including in, e.g., V1) could parsimoniously explain positive and negative SZ symptoms (13), including, e.g., unstable or spontaneous percepts and deficient short-term memory.

Directly testing a neuronal "attractor" theory in human samples is not currently feasible, because it requires recording the activity of large populations of neurons with single-cell resolution in an intact brain. Two-photon calcium imaging (2P-Ca^{2+}) affords this level of analysis in awake mice, and, using different mouse models of SZ, we previously tested whether unreliable ensemble activations, a possible signature of inherent cortical attractor degradation, could be a feasible downstream intersection point of SZ causal pathways (14). We examined both an NMDA receptor (NMDAR) hypofunction model and a 22q11.2 microdeletion model (i.e., a penetrant risk genotype for SZ) using adult mice. Despite some cell-level differences, in both mouse models ensemble activity patterns in local neuronal populations were similarly disorganized (i.e., less reliable) in the visual cortex. While this work is encouraging and is consistent with 2 independent studies using NMDAR hypofunction models (15,16), the need to examine ensemble activity in additional models of SZ risk pathways is critical to testing the hypothesis of convergence and the attractor theory of SZ.

Here we examined whether and how a recently identified SZ risk gene, *SETD1A* (17,18), could contribute to the sensory processing phenotypes seen in SZ via a disorganization of cortical ensembles. *SETD1A* is a lysine methyltransferase, which methylates histones with modulatory effects on a large number of genes expressed brain wide (18), but especially in the neocortex (19). Mice carrying a heterozygous loss-of-function mutation in *Setd1a* (i.e., *Setd1a*$^{+/-}$) have recently been shown to exhibit alterations in axonal branching, synaptic plasticity, and neuronal excitability in the PFC as well deficits in working memory that were reversed by blocking LSD1, a lysine demethylase that counters the effects of *Setd1a* (19).

We measured neural population dynamics in the V1 of *Setd1a*$^{+/-}$ mice with 2P-Ca^{2+} and local field potential (LFP) recordings to test 1) whether this model of a novel risk genotype also exhibits sensory-processing phenotypes, validating its utility for understanding such aberrations in neuropsychiatric diseases; 2) whether *Setd1a*$^{+/-}$ mice, like other models of SZ-relevant disease processes, showed a disruption of cortical ensembles, lending further weight to an altered ensemble hypothesis of SZ; and 3) whether ensemble dysfunction in *Setd1a*$^{+/-}$ co-occurs with aberrant local oscillations within and between cortical layers, combining spatiotemporal with frequency-temporal information to provide a more complete understanding of circuit alterations.

METHODS AND MATERIALS

Animals

We used a mouse model carrying a *Setd1a* loss-of-function allele (Figure 1C; Supplemental Methods). Experiments were carried out on 10 *Setd1a*$^{+/-}$ mice and 10 littermate/cagemate control mice (male only, 23–30 g, age 8–14 weeks). All animal procedures were carried out in accordance with and approved by the Columbia University Institutional Animal Care and Use Committee.

Surgery

Virus injection, head plate fixation, and craniotomies were carried out in that order over the course of 3 weeks as previously described (14). Details are provided in Supplemental Methods.

Two-Photon Calcium Imaging

The activity of cortical neurons was recorded by imaging fluorescence (F) changes under a 2-photon microscope (Bruker, Billerica, MA) excited with a Ti:Sapphire laser (Chameleon Ultra II [Coherent, Santa Clara, CA] or Mai Tai HP Deep See [Spectra Physics, Santa Clara, CA]) tuned at 940 nm and scanned with resonant galvometers through a ×20 (numerical aperture 0.9) water immersion objective (Olympus, Center Valley, PA). Resonant scanning and image acquisition were controlled by PrairieView (Bruker, Billerica, MA) software (10 frames per second for 256 × 256 pixels, 200–225 μm beneath the pial surface). Imaging consisted of a visual stimulation condition (15 minutes), followed by 20–40 minutes of awake rest in a dark room with the monitor off, followed by a second visual stimulation. Data are reported on 9 wild-type (WT) and 9 *Setd1a*$^{+/-}$ mice (2 mice were excluded from this phase owing to insufficient virus expression, but they were used for LFP recordings). Sessions started at the same time of day for all mice (between 11 AM and 4 PM). Locomotion was inferred from deflections in an infrared LED per photo-darlington pair (Figure 1A), which were converted to a voltage trace and aligned to the image acquisition.

Visual Stimulation

Visual stimuli were generated using the Psychophysics Toolbox in MATLAB (The Mathworks, Inc., Natick, MA) and displayed on a LCD monitor (19-inch diagonal, 60-Hz refresh rate) positioned 15 cm from the right eye at 45° to the long axis of the animal (Figure 1A). Stimuli were full-field square-wave gratings (100% contrast, 0.04 cycles per degree, 2.0 cycles per second) drifting in 12 different directions in random order presented for 3 seconds, followed by an interstimulus interval of 7–8 seconds of mean luminescence gray screen. Across sessions, mice saw a total of 14 presentations of each stimulus.

Local Field Potential Recordings

LFPs were recorded from a single contact from a 16-channel linear silicon probe (spaced at 50-μm intervals; model a1×16–3mm50–177; NeuroNexus, Ann Arbor, MI) in V1. Data are reported on 8 WT and 8 *Setd1a*$^{+/-}$ mice (4 mice were excluded due to breaking of the coverslip during the final surgery). Mice viewed visual stimuli (described above) and LFP data were preprocessed (Supplemental Methods) and converted to current source densities (CSDs) (6,20). Uninterpolated single-trial CSDs were used for all subsequent analyses.

Image Analysis

Imaging datasets were scored similarly to previous reports (14,21). Subsequent analyses focused on the positive discrete first derivative of halo-subtracted regions of interest semi-manually selected from motion corrected calcium imaging datasets (22) (Supplemental Methods).

Single-Cell Analyses

For each neuron, we estimated events using thresholds set as 3.1 SD ($p < .001$) above baseline (ΔF)/F for each neuron (lower 8% of values) (14,23), scoring from the beginning to the end of each cross above the threshold as 1 full event. We first quantified the average number of events per minute and the average duration of events. Note that decay time had a minimal effect on calcium transient duration or rate because the positive first derivative (increases in fluorescence) made up ΔF/F. Average rate and duration were computed for each mouse, followed by 2-sample 2-tailed *t* tests.

Pairwise Analysis

Pairwise coactivity between single cells was assessed by calculating Pearson correlations of ΔF/F values between cell pairs for the entire rest period, for frames with locomotion, and for "ensemble activations" (Supplemental Methods). Differences in spatial gradients of intercell correlations were assessed with a 2-way mixed analysis of variance with space (10 spatial bins) as the within-group factor and group (WT × *Setd1a*$^{+/-}$) as the between-group factor.

Population Analysis

Population level analyses of ongoing activity assessed the correlations of population activity patterns between cortical "ensemble activations," or time frames with significant levels of coactivity, occurring throughout the imaging session. This involved 4 steps: identification of ensemble activations, t-distributed stochastic neighbor embedding (*t*-SNE) sorting, k-means cluster analyses, and statistical comparisons (Supplemental Methods).

Analysis of Stimulus-Evoked Activity: Single Cell

The ΔF values were averaged within trials (free of locomotion ± 2 seconds) from stimulus onset to offset and across trials of the same stimulus (held at 5 trials per stimulus across mice). Analyses focused on cells exhibiting significant stimulus-evoked activity (Supplemental Methods). The orientation selectivity index and direction selectivity index were calculated on average ΔF responses (14,24) and were compared with *t* tests either 1) after averaging within mice (9 vs. 9 estimates) or 2) at the single-cell level. These approaches yielded the same effects. For plotting purposes, responses across the 12 directions were fit with 1 (Figure 1N, O) or 2 Gaussians to estimate the "true" preferred orientation (7).

Analysis of Stimulus-Evoked Activity: Population Level

The same cell-cell correlation analyses and ensemble-activation analyses were carried out on data collected during visual stimulation as on data collected during rest. In addition, support vector machine analyses were used to test the reliability of V1 population coding of visual stimuli; these analyses are described in Supplemental Methods.

Analysis of LFP/CSD Oscillations

We converted CSD waveforms from single trials from each contact to time-frequency spectra using a modified Morlet wavelet convolution (2–110 Hz, 1-Hz steps, 1–14 cycles, 5-

msec steps from −500 to 3500 msec after stimulus onset, 500 msec after offset), focusing on the first 20 trials (6,14,25–28).

First we calculated average stimulus-induced power (squared absolute power of complex Morlet result [dB], subtracting the 500 msec prestimulus baseline) focusing on putative layer 2/3 response dynamics (since the 2P-Ca^{2+} recordings covered cells from this layer) by averaging over 4 adjacent contacts from this putative region. We compared WT and *Setd1a* $^{+/-}$ mice with 2-sample 2-tailed *t* tests for 12 time-frequency bins (1–500 msec [early] and 500–2000 msec after stimulus [sustained] for 6 bands) (3,29–33) (Supplemental Methods). Surrogate-corrected phase coherence values from WT and *Setd1a*$^{+/-}$ mice were compared with 2-sample 2-tailed *t* tests carried out for all electrode pairs and frequencies.

RESULTS

Normal Neuronal Activity Levels in Primary Visual Cortex in *Setd1a*$^{+/-}$ Mice

Awake WT and *Setd1a*$^{+/-}$ mice were accustomed to head fixation on a rotating treadmill (Figure 1A) and placed in a darkened room in front of an LCD monitor presenting a blank screen (~20–30 minutes) or full-field grating stimuli (Figure 1B). The proportion of time spent running did not differ between mouse groups (Figure 1C), and LFP recordings showed similar distributions of spectral power across low- and high-frequency bands, indicating no obvious differences in gross arousal between groups (34,35). 2P-CA^{2+} with panneuronally expressed calcium indicator GCaMP6s was performed in putative monocular primary visual cortex as a proxy of firing activity of layer 2/3 neurons in WT (Figure 1F, G) and *Setd1a*$^{+/-}$ (Figure 1H, I) mice during resting activity (awake, nonlocomotive). The average activity of individual neurons did not differ between mouse groups when quantified as average number of calcium events or their duration (Figure 1J, K). The relative distributions and relationships between these variables were equivalent between WT and *Setd1a*$^{+/-}$ mice (Figure 1L). The proportion of visually driven neurons (Supplemental Methods) did not differ between WT and *Setd1a*$^{+/-}$ mice (Figure 1M). Of the responsive neurons, WT and *Setd1a*$^{+/-}$ mice did not differ in orientation selectivity (7,14) at the cell level (Figure 1N, O) or when averaged within mice (Supplemental Figure S1A). Direction selectivity also did not differ at the single-neuron level when assessed as mousewise or cellwise averages (Supplemental Figure S1B, C). Thus, *Setd1a*$^{+/-}$ on the whole did not exhibit altered single neuronal responses in V1, a result both similar to (22q11.2 microdeletion) and distinct from (NMDAR hypofunction) other models of SZ-relevant disease processes (14).

Ensemble Activations Are Abnormal in *Setd1a*$^{+/-}$ Mice During Ongoing Activity

We next examined the correlated activity of populations of neurons in V1 present during rest and locomotion. Figure 2A, B shows raster plots of neuronal activity in 2 representative mice. Locomotion (indicated by gray bars) coincided with increases in coactivity among a large number of V1 neurons, as previously described (36). Locomotion bouts evoked similar magnitudes of network activity between WT and *Setd1a*$^{+/-}$ mice (proportion of full network activation [i.e., all neurons showing max ΔF]: WT = 0.10 ± 0.3, *Setd1a*$^{+/-}$ = 0.09 ± 0.02; t_{16} = 0.73, p = .47) (Supplemental Figure S2A).

Between bouts of locomotion, we also observed ensemble activations, statistically defined periods with significant coactivity in the local network (indicated by the black bars in Figure 2A, B) (14). WT and *Setd1a*$^{+/-}$ mice did not differ in the rate (Supplemental Figure S2B) or magnitude (Supplemental Figure S2C) of ensemble activations during the resting recording period (activations per min: WT = 7.24 ± 1.87, *Setd1a*$^{+/-}$ = 8.18 ± 3.8, $t_{16} = -0.56$, $p = .57$; magnitude: WT = 0.15 ± 0.3, *Setd1a*$^{+/-}$ = 0.14 ± 0.01, $t_{16} = 1.25$, $p = .22$).

Analyzing average correlations between all pairs of neurons showed that *Setd1a*$^{+/-}$ mice also did not significantly differ from WT mice at the level of gross correlated activity regardless of network states (i.e., locomotion, ensemble activations, or all rest frames; all $p > .10$) (Figure 2C). But, interestingly, the spatial distribution of correlations, determined by binning cell-cell pairs based on their intersoma distances (Figure 2D), showed that the spatial gradient of correlations in layer 2/3 was shallower in *Setd1a*$^{+/-}$ mice during the ensemble activations (Figure 2D) ($F^{space\times group}_{1,9} = 2.06$, $p < .05$). This effect was relatively small, however, and did not hold for locomotion periods ($F^{space\times group}_{1,9} = 1.06$, $p = .39$). When all rest-period data were pooled, the effect remained ($F^{space\times group}_{1,9} = 2.09$, $p < .05$). Although this shift in the spatial distribution of functional correlations could arise from a variety of circuit-level alterations (e.g., weaker surround inhibition, imbalanced local vs. global excitatory inputs, altered circuit dynamics), altogether it suggests that *Setd1a*$^{+/-}$ mice have altered neuronal networks, rather than even changes in synaptic strength, neuronal responses, and/or cortical arousal (10).

To test this, we focused on the population activity patterns inherent in ensemble activations, defined as coactive groups of neurons (Figure 2E), first reducing the multineuronal patterns to 3-dimensional *t*-SNE space (Figure 2F) and then carrying out a k-means clustering analysis to identify similar reactivations of groups of neurons over time (sorted in Figure 2E). For WT mice, resting period ensemble activations formed clearly separated clusters in *t*-SNE space (Figure 2F), indicating distinct and reliable attractor-like patterns made up of coactivated ensembles of neurons identifiable in the sorted raster plot (Figure 2E) and as previously shown (37,38). In *Setd1a*$^{+/-}$ mice, on the other hand, ensemble activation patterns were seemingly random, showing little clustering in *t*-SNE space (Figure 2G, H) and an apparent lack of cortical attractors (12,14). Combining estimates of normalized within-activity pattern correlations (r^{WCN}) across mice while varying the number of "clusters" in the fitted solution (Figure 2I) ($F^{numclus\times group}_{1,5} = 2.53$, $p < .05$) or fixing it to 3 per 100 cells (the average across mice) (Figure 2J) ($t_{16} = 2.82$, $p < .05$) showed that this effect was statistically robust in the sample, although both WT and *Setd1a*$^{+/-}$ mice showed evidence of some organized ensemble activity relative to a time-shuffled surrogate (indicated in red in Figure 2I, J).

In line with previous observations (39), ensemble activations were not strongly spatially clustered and thus could not be simply explained by the subtle changes in correlation gradients described above (Supplemental Results; Supplemental Figure S2D–F).

Ensemble Disorganization in *Setd1a*$^{+/-}$ Mice During Visual Processing

Disorganized ensemble activity was also present during visual stimulation in *Setd1a*$^{+/-}$. Cell pairs in V1 of *Setd1a*$^{+/-}$ showed a deficit in the spatial distribution of correlations (Figure

3A) ($F^{space\times group}_{1,9} = 1.95$, $p < .05$) and a decrease in the robustness of ensemble activations during visual stimulation (00) ($F^{numclus\times group}_{1,5} = 3.01$, $p < .05$; $t_{16} = 1.40$, $p = .09$) similar to rest. We then examined whether this disorganization could affect how V1 networks reliably encode visual stimuli. We calculated the correlations between the population activation patterns for each trial pair and averaged trial-trial pair types for each stimulus orientation/direction to construct a correlation matrix (organized with orthogonal stimulus orientations/directions adjacent to each other, creating a checkerboard pattern) (14). In WT mice, these matrices indicated clear differentiations in the population representations of different visual stimuli (Figure 3B). In *Setd1a*$^{+/\hat{R}}$ mice, although visual stimuli in general evoked reliable responses, the checkerboard pattern was ostensibly less defined, as both similar and different stimulus orientation/directions showed high relative correlations, suggesting that visually driven ensembles do not reliably differentiate separate stimuli (Figure 2G, H). To test this, we used machine learning to examine how reliably V1 populations could differentiate between stimuli in each mouse. Using the first 5 presentations of each stimulus direction, we used a support vector machine to construct linear classifier models for each stimulus direction using the population activity (26,40,41). The accuracy and performance (d-prime) of these models did not differ between WT and *Setd1a*$^{+/-}$ mice when they were applied to the data they were trained on (Supplemental Figure S3F–I), suggesting that the algorithms equally and adequately produced models that represented the population response to the specific stimuli on a given trial. However, when the models were applied to the subsequent presentations of the visual stimuli, the models generated from *Setd1a*$^{+/-}$ mice performed significantly worse (Figure 3C, D) regarding both sensitivity (d-prime, at classifier score cutoff of $z = 2.3$: $t_{16} = 3.30$, $p < .01$) and the overall accuracy of the models combined ($t_{16} = 2.32$, $p < .05$). That is, the stimuli viewed by mice were less reliably decoded from V1 neuronal populations in *Setd1a*$^{+/-}$ mice. Interestingly, unaffected orientation selectivity index and direction selectivity index (Figure 1M–O), which reflect trial-averaged stimulus selectivity in individual neurons, suggest that these effects reflect an ensemble pathology, involving altered trial-to-trial reliability of distinct neuronal coactivation patterns (Figure 2G; Supplemental Figure S3A).

Ensemble Disorganization in *Setd1a*$^{+/-}$ Mice Co-occurs With Disrupted Oscillations

LFP oscillations spanning multiple frequencies have been recorded intracortically as well as at the scalp (by electroencephalography [EEG]), showing remarkably conserved frequency bands across techniques, regions, and species (42) and reflecting a fundamental feature of how cortical ensembles organize in time (43). Given the spatiotemporal circuit aberrations that we observed (above), we wondered whether mutant mice also had frequency-temporal aberrations, potentially mirroring abnormalities found in some neuropsychiatric samples (3,31,33,44,45). In the same mice used for the 2P-Ca^{2+} experiments, we independently recorded LFPs using 16-channel perpendicular silicon probes in V1 (spanning 750 μm of cortical depth) (Figure 4A). To focus on dynamics within layer 2/3 (20,46), CSD profiles (Figure 4B–E) were analyzed to detect stimulus-induced changes in oscillatory power (Figure 4F, G). Examination of these power plots suggested that *Setd1a*$^{+/-}$ mice showed reduced high-gamma power (70–110 Hz) in the early-onset response (2.43, $p < .05$) (Figure 4H). Furthermore, the sustained alpha-band (8–14 Hz) desynchronization known to

accompany active visual processing (30,47) was also reduced in *Setd1a*$^{+/-}$ mice in layer 2/3 (t_{16} = 2.23, p < .05) (Figure 4I).

These reductions in alpha/gamma power may suggest altered local synchrony in these bands in layer 2/3. We further assessed whether interlaminar coherence (a measure independent of power) could further support this interpretation. We focused on the central contact of putative layer 2/3 (i.e., 200 μm from the surface, the "seed") and calculated instantaneous interelectrode phase-phase synchrony for stimulus-induced activity (i.e., with other depths) for 1–110 Hz (Figure 4J). *Setd1a*$^{+/-}$ mice showed markedly reduced phase synchrony between layers 2/3 and 5 in the alpha and gamma frequency bands (Figure 4K), suggesting a disruption of spatially coherent neuronal activity in these disease-relevant bandwidths in V1.

DISCUSSION

We identified aberrant ensemble activity and oscillations in V1 cortical circuits of adult mice with a loss-of-function mutation in the *Setd1a* gene (17,18). Altered cortical activity consisted of loss of well-defined, correlated activity patterns in layer 2/3 neuronal populations, resulting in a less reliable encoding of visual stimuli at the population level. We found this effect on cortical ensemble activity despite absent or relatively subtle effects on single-neuron activity or pairwise correlations. These circuit abnormalities occurred along with decreases in local and intralaminar oscillatory synchrony in V1, suggesting both time-space and time-frequency dimensions of circuit disruptions. Altogether these findings 1) highlight a cortical phenotype resulting from *Setd1a* deficiency affecting sensory processing circuits, adding to previous findings regarding PFC anatomy and PFC-dependent behaviors (19), 2) offer circuit-level insight into the underlying nature of sensory-processing dysfunction seen in neuropsychiatric disorders, and 3) provide new evidence for an ensemble theory of SZ pathophysiology.

Visual Cortical Abnormalities in *Setd1a*$^{+/-}$ Mice

Loss-of-function mutations in the *SETD1A* gene are relatively rare in humans, being present in <0.5% of the population, but they carry substantial risk for the development of SZ (44, 45). The protein SETD1A is part of the SET/COMPASS complex, which mediates mono-, di-, and trimethylation of lysine 4 on the histone H3 protein (H3K4) (18). Given that this protein affects the expression of hundreds of genes throughout all stages of development, it is unclear from genetic studies alone how loss-of-function mutations could contribute to cortical pathophysiology relevant to SZ.

One recent study (19) made significant strides to this end, showing that a large number of putative *SETD1A* direct chromatin targets appear to have a cortex- and neuronal-specific function in both mice and humans, and that SETD1A deficiency in mice leads to sparser structural connectivity owing to alterations in axon arborization, short-term synaptic plasticity, and neuronal excitability, collectively leading to disruptions of network activities that support working memory and related cognitive operations. Interestingly, reinstatement of *SETD1A* expression in adulthood or pharmacological antagonism of LSD1, a counteracting demethylase for *SETD1A*, results in a rescue of the working memory deficits in SETD1A deficiency. These findings have focused primarily on PFC tissue and PFC-

dependent behaviors, yet SZ is known to have cortical pathophysiology affecting nearly all neocortical structures. This includes structural and functional deficits in visual cortex and related perceptual aberrations (4,5,48). Our results in the present study demonstrate that SETD1A-related neuropathology also extends to primary sensory cortices, highlighting that this mouse model may be additionally useful for understanding and developing treatments for perceptual deficits in SZ. Further exploration of other cortical regions, comparing ensemble dynamics and region-relevant behavioral effects, will be valuable for understanding the effects of SETD1A deficiency. One caveat of the present study is the use of only male mice, especially given the sexually dimorphic nature of the cortex (49) and the course and features of SZ (50). Future work testing whether and which phenotypic differences present in female *Setd1a*$^{+/-}$ mice as well will be of significant basic and translational value.

Schizophrenia as a Disease of Cortical Ensembles

An “ensemble hypothesis of SZ” would posit that the hundreds of candidate genetic, molecular, and cell-level risk pathways identified in SZ actually converge across patients downstream at the multicellular level, essentially undermining the reliability of ensemble activity and plasticity in a manner that is both similar across cases (despite different genetic causes) and fundamental to SZ (9,14). Such a breakdown of neuronal ensembles would compromise signal propagation among larger brain networks, affecting more complex information processing underlying cognition and behavioral control (10).

Studies assessing the downstream effects of SZ-relevant molecular/genetic alterations have identified decreases in reliability of ensemble activity patterns across models despite differences at the level of gross synchrony (i.e., LFPs), single-neuron activity levels, and pairwise correlations (14–16). We identified an equivalent pattern of activity deficits in V1 of *Setd1a*$^{+/-}$ mice (Figure 5), adding further evidence to this “ensemble” hypothesis.

Also, in the same local regions of V1, we identified abnormalities in alpha- and gamma-band oscillatory dynamics, as well as changes in intralaminar coherence in these frequencies (Figure 4), bringing up some hypotheses regarding relationships between time-space and time-frequency dynamics of cortical ensembles (Supplemental Results and Discussion). While EEG recorded at the human scalp undoubtedly has a different relationship to underlying cortical populations from mouse intracortical LFP/EEG, the fact that some EEG studies in neuropsychiatric samples have found similar aberrations (3,31,33,44,45) suggest that *Setd1a*$^{+/-}$ mice are a valuable model for exploring these biomarkers, especially if scalp EEG and intracortical LFP oscillations reflect the same essential underlying neurophysiological mechanisms.

Significant work nevertheless remains to address an ensemble hypothesis of SZ. Future studies should compare additional models of SZ-relevant disease processes, contrast additional models of other diseases (e.g., autism spectrum or depression models), assess the developmental trajectory of ensemble maturation in health and disease [since SZ has a well-defined developmental component (51)], and assess the ability of optogenetic ensemble manipulations (52,53) to directly rescue cognitive and perceptual deficits in relevant animal models.

Supplementary Material

Refer to Web version on PubMed Central for supplementary material.

ACKNOWLEDGMENTS AND DISCLOSURES

This work was supported by the National Institutes of Health (Grant Nos. R00MH115082 [to JPH], R01MH080234 [to JAG], R01EY011787 [to RY], and R01MH115900 [to RY]). RY is an Ikerbasque Research Professor at the Donostia International Physics Center.

REFERENCES

1. Javitt DC, Freedman R (2015): Sensory processing dysfunction in the personal experience and neuronal machinery of schizophrenia. Am J Psychiatry 172:17–31. [PubMed: 25553496]
2. Hamm JP, Gilmore CS, Picchetti NA, Sponheim SR, Clementz BA (2011): Abnormalities of neuronal oscillations and temporal integration to low- and high-frequency auditory stimulation in schizophrenia. Biol Psychiatry 69:989–996. [PubMed: 21216392]
3. Spencer KM, Nestor PG, Perlmutter R, Niznikiewicz MA, Klump MC, Frumin M, et al. (2004): Neural synchrony indexes disordered perception and cognition in schizophrenia. Proc Natl Acad Sci U S A 101:17288–17293. [PubMed: 15546988]
4. Glantz LA, Lewis DA (2000): Decreased dendritic spine density on prefrontal cortical pyramidal neurons in schizophrenia. Arch Gen Psychiatry 57:65–73. [PubMed: 10632234]
5. Hashimoto T, Bazmi HH, Mirnics K, Wu Q, Sampson AR, Lewis DA (2008): Conserved regional patterns of GABA-related transcript expression in the neocortex of subjects with schizophrenia. Am J Psychiatry 165:479–489. [PubMed: 18281411]
6. Hamm JP, Yuste R (2016): Somatostatin interneurons control a key component of mismatch negativity in mouse visual cortex. Cell Rep 16:597–604. [PubMed: 27396334]
7. Niell CM, Stryker MP (2008): Highly selective receptive fields in mouse visual cortex. J Neurosci 28:7520–7536. [PubMed: 18650330]
8. Huberman AD, Niell CM (2011): What can mice tell us about how vision works? Trends Neurosci 34:464–473. [PubMed: 21840069]
9. Gogos JA, Crabtree G, Diamantopoulou A (2019): The abiding relevance of mouse models of rare mutations to psychiatric neuroscience and therapeutics [published online ahead of print Apr 12]. Schizophr Res.
10. Krystal JH, Anticevic A, Yang GJ, Dragoi G, Driesen NR, Wang X-J, Murray JD (2017): Impaired tuning of neural ensembles and the pathophysiology of schizophrenia: A translational and computational neuroscience perspective. Biol Psychiatry 81:874–885. [PubMed: 28434616]
11. Yuste R (2015): From the neuron doctrine to neural networks. Nat Rev Neurosci 16:487–497. [PubMed: 26152865]
12. Rolls ET, Loh M, Deco G, Winterer G (2008): Computational models of schizophrenia and dopamine modulation in the prefrontal cortex. Nat Rev Neurosci 9:696–709. [PubMed: 18714326]
13. Adams RA, Napier G, Roiser JP, Mathys C, Gilleen J (2018): Attractor-like dynamics in belief updating in schizophrenia. J Neurosci 38:9471–9485. [PubMed: 30185463]
14. Hamm JP, Peterka DS, Gogos JA, Yuste R (2017): Altered cortical ensembles in mouse models of schizophrenia. Neuron 94:153–167.e8. [PubMed: 28384469]
15. Liang B, Zhang L, Barbera G, Fang W, Zhang J, Chen X, et al. (2018): Distinct and dynamic ON and OFF neural ensembles in the prefrontal cortex code social exploration. Neuron 100:P700–P714.e9.
16. Seshadri S, Klaus A, Winkowski DE, Kanold PO, Plenz D (2018): Altered avalanche dynamics in a developmental NMDAR hypofunction model of cognitive impairment. Transl Psychiatry 8:3. [PubMed: 29317600]
17. Singh T, Kurki MI, Curtis D, Purcell SM, Crooks L, McRae J, et al. (2016): Rare loss-of-function variants in *SETD1A* are associated with schizophrenia and developmental disorders. Nat Neurosci 19:571–577. [PubMed: 26974950]

18. Takata A, Xu B, Ionita-Laza I, Roos JL, Gogos JA, Karayiorgou M (2014): Loss-of-function variants in schizophrenia risk and *SETD1A* as a candidate susceptibility gene. Neuron 82:773–780. [PubMed: 24853937]
19. Mukai J, Cannavò E, Crabtree GW, Sun Z, Diamantopoulou A, Thakur P, et al. (2019): Recapitulation and reversal of schizophrenia-related phenotypes in SETD1A-deficient mice. Neuron 104:471–487. e12. [PubMed: 31606247]
20. Buzsáki G, Anastassiou CA, Koch C (2012): The origin of extracellular fields and currents—EEG, ECoG, LFP and spikes. Nat Rev Neurosci 13:407–420. [PubMed: 22595786]
21. Chen T-W, Wardill TJ, Sun Y, Pulver SR, Renninger SL, Baohan A, et al. (2013): Ultrasensitive fluorescent proteins for imaging neuronal activity. Nature 499:295–300. [PubMed: 23868258]
22. Dubbs A, Guevara J, Yuste R (2016): Moco: Fast motion correction for calcium imaging. Front Neuroinform 10:6. [PubMed: 26909035]
23. Carrillo-Reid L, Miller J-EK, Hamm JP, Jackson J, Yuste R (2015): Endogenous sequential cortical activity evoked by visual stimuli. J Neurosci 35:8813–8828. [PubMed: 26063915]
24. Mazurek M, Kager M, van Hooser SD (2014): Robust quantification of orientation selectivity and direction selectivity. Front Neural Circuits 8:92. [PubMed: 25147504]
25. Hamm JP, Ethridge LE, Shapiro JR, Stevens MC, Boutros NN, Summerfelt AT, et al. (2012): Spatiotemporal and frequency domain analysis of auditory paired stimuli processing in schizophrenia and bipolar disorder with psychosis. Psychophysiology 49:522–530. [PubMed: 22176721]
26. Agetsuma M, Hamm JP, Tao K, Fujisawa S, Yuste R (2017): Parvalbumin-positive interneurons regulate neuronal ensembles in visual cortex. Cereb Cortex 6:1–15.
27. Hamm JP, Dyckman KA, McDowell JE, Clementz BA (2012): Pre-cue fronto-occipital alpha phase and distributed cortical oscillations predict failures of cognitive control. J Neurosci 32:7034–7041. [PubMed: 22593071]
28. Kozai TDY, Du Z, Gugel ZV, Smith MA, Chase SM, Bodily LM, et al. (2015): Comprehensive chronic laminar single-unit, multi-unit, and local field potential recording performance with planar single shank electrode arrays. J Neurosci Methods 242:15–40. [PubMed: 25542351]
29. Hanslmayr S, Aslan A, Staudigl T, Klimesch W, Herrmann CS, Bäuml K-H (2007): Prestimulus oscillations predict visual perception performance between and within subjects. Neuroimage 37:1465–1473. [PubMed: 17706433]
30. Capotosto P, Babiloni C, Romani GL, Corbetta M (2009): Frontoparietal cortex controls spatial attention through modulation of anticipatory alpha rhythms. J Neurosci 29:5863–5872. [PubMed: 19420253]
31. Tan H-RM, Lana L, Uhlhaas PJ (2013): High-frequency neural oscillations and visual processing deficits in schizophrenia. Front Psychol 4:621. [PubMed: 24130535]
32. Revheim N, Corcoran CM, Dias E, Hellmann E, Martinez A, Butler PD, et al. (2014): Reading deficits in schizophrenia and individuals at high clinical risk: Relationship to sensory function, course of illness, and psychosocial outcome. Am J Psychiatry 171:949–959. [PubMed: 25178752]
33. Martínez A, Gaspar PA, Hillyard SA, Bickel S, Lakatos P, Dias EC, Javitt DC (2015): Neural oscillatory deficits in schizophrenia predict behavioral and neurocognitive impairments. Front Hum Neurosci 9:371. [PubMed: 26190988]
34. Harris KD, Thiele A (2011): Cortical state and attention. Nat Rev Neurosci 12:509–523. [PubMed: 21829219]
35. Vinck M, Batista-Brito R, Knoblich U, Cardin JA (2015): Arousal and locomotion make distinct contributions to cortical activity patterns and visual encoding. Neuron 86:740–754. [PubMed: 25892300]
36. Niell CM, Stryker MP (2010): Modulation of visual responses by behavioral state in mouse visual cortex. Neuron 65:472–479. [PubMed: 20188652]
37. Carrillo-Reid L, Kang J-E, Hamm JP, Jackson J, Yuste R, Miller J-EK, et al. (2015): Endogenous sequential cortical activity evoked by visual stimuli. J Neurosci 35:8813–8828. [PubMed: 26063915]
38. Luczak A, Barthó P, Harris KD (2009): Spontaneous events outline the realm of possible sensory responses in neocortical populations. Neuron 62:413–425. [PubMed: 19447096]

39. Miller J-EK, Ayzenshtat I, Carrillo-Reid L, Yuste R (2014): Visual stimuli recruit intrinsically generated cortical ensembles. Proc Natl Acad Sci U S A 111:E4053–E4061. [PubMed: 25201983]
40. Wenzel M, Han S, Smith EH, Hoel E, Greger B, House PA, Yuste R (2019): Reduced repertoire of cortical microstates and neuronal ensembles in medically induced loss of consciousness. Cell Syst 8:467–474.e4. [PubMed: 31054810]
41. Christianini N, Shawe-Taylor JC (2000): An Introduction to Support Vector Machines and Other Kernel-Based Learning Methods. Cambridge, UK: Cambridge University Press.
42. Buzsáki G, Logothetis N, Singer W (2013): Scaling brain size, keeping timing: Evolutionary preservation of brain rhythms. Neuron 80:751–764. [PubMed: 24183025]
43. Buzsaki G (2009): Rhythms of the Brain. New York: Oxford University Press.
44. Haenschel C, Linden DE, Bittner RA, Singer W, Hanslmayr S (2010): Alpha phase locking predicts residual working memory performance in schizophrenia. Biol Psychiatry 68:595–598. [PubMed: 20673879]
45. Uhlhaas PJ, Roux F, Rodriguez E, Rotarska-Jagiela A, Singer W (2010): Neural synchrony and the development of cortical networks. Trends Cogn Sci 14:72–80. [PubMed: 20080054]
46. Kajikawa Y, Schroeder CE (2011): How local is the local field potential? Neuron 72:847–858. [PubMed: 22153379]
47. Klimesch W, Sauseng P, Hanslmayr S (2007): EEG alpha oscillations: The inhibition-timing hypothesis. Brain Res Rev 53:63–88. [PubMed: 16887192]
48. Chen Y (2011): Abnormal visual motion processing in schizophrenia: A review of research progress. Schizophr Bull 37:709–715. [PubMed: 21436317]
49. Luders E, Toga AW (2010): Sex differences in brain anatomy. Prog Brain Res 186:2–12.
50. Abel KM, Drake R, Goldstein JM (2010): Sex differences in schizophrenia. Int Rev Psychiatry 22:417–428. [PubMed: 21047156]
51. Jaaro-Peled H, Hayashi-Takagi A, Seshadri S, Kamiya A, Brandon NJ, Sawa A (2009): Neurodevelopmental mechanisms of schizophrenia: Understanding disturbed postnatal brain maturation through neuregulin-1–ErbB4 and DISC1. Trends Neurosci 32:485–495. [PubMed: 19712980]
52. Marshel JH, Kim YS, Machado TA, Quirin S, Benson B, Kadmon J, et al. (2019): Cortical layer–specific critical dynamics triggering perception. Science 365(6453):eaaw5202. [PubMed: 31320556]
53. Carrillo-Reid L, Han S, Yang W, Akrouh A, Yuste R (2019): Controlling visually guided behavior by holographic recalling of cortical ensembles. Cell 178:447–457.e5. [PubMed: 31257030]
54. Uhlhaas PJ (2011): High-frequency oscillations in schizophrenia. Clin EEG Neurosci 42:77–82. [PubMed: 21675597]
55. Moran LV, Hong LE (2011): High vs. low frequency neural oscillations in schizophrenia. Schizophr Bull 37:659–663. [PubMed: 21653278]

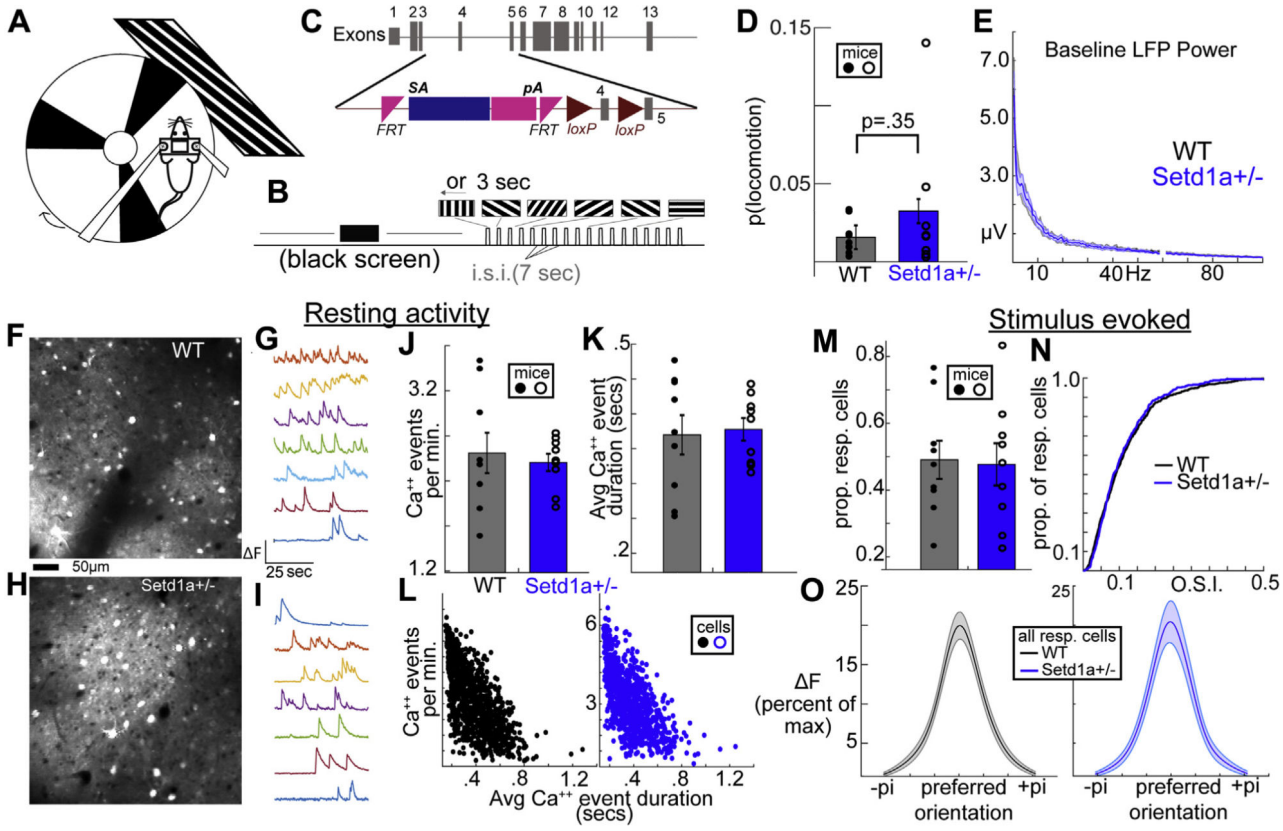

Figure 1.

Arousal, locomotion, and neuronal activity levels are unaffected in *Setd1a*$^{+/-}$ mice. **(A, B)** Head-fixed mice on a circular treadmill viewed either full field visual grating stimuli or a blank screen in a dark room. **(C)** Mice with a loss-of-function mutation in *Setd1a* were compared with WT littermate/cagemate control mice. **(D, E)** *Setd1a*$^{+/-}$ mice showed time spent locomoting and baseline LFP power distributions equivalent to WT mice. **(F–I)** Two-photon calcium imaging enabled the quantification of activity levels in single neurons, revealing **(J)** unaffected rate and **(K)** size of Ca^{2+} events. **(L)** These measures showed similar distributions and relationships between WT and *Setd1a*$^{+/-}$ mice. Furthermore, the **(M, N)** proportions of visually driven cells and **(O)** their orientation selectivity were unaffected in *Setd1a*$^{+/-}$ mice. Avg, average; FRT, flippase recognition target; LFP, local field potential; pi, 3.1415926; prop. resp., proportion of responsive cells; WT, wild-type.

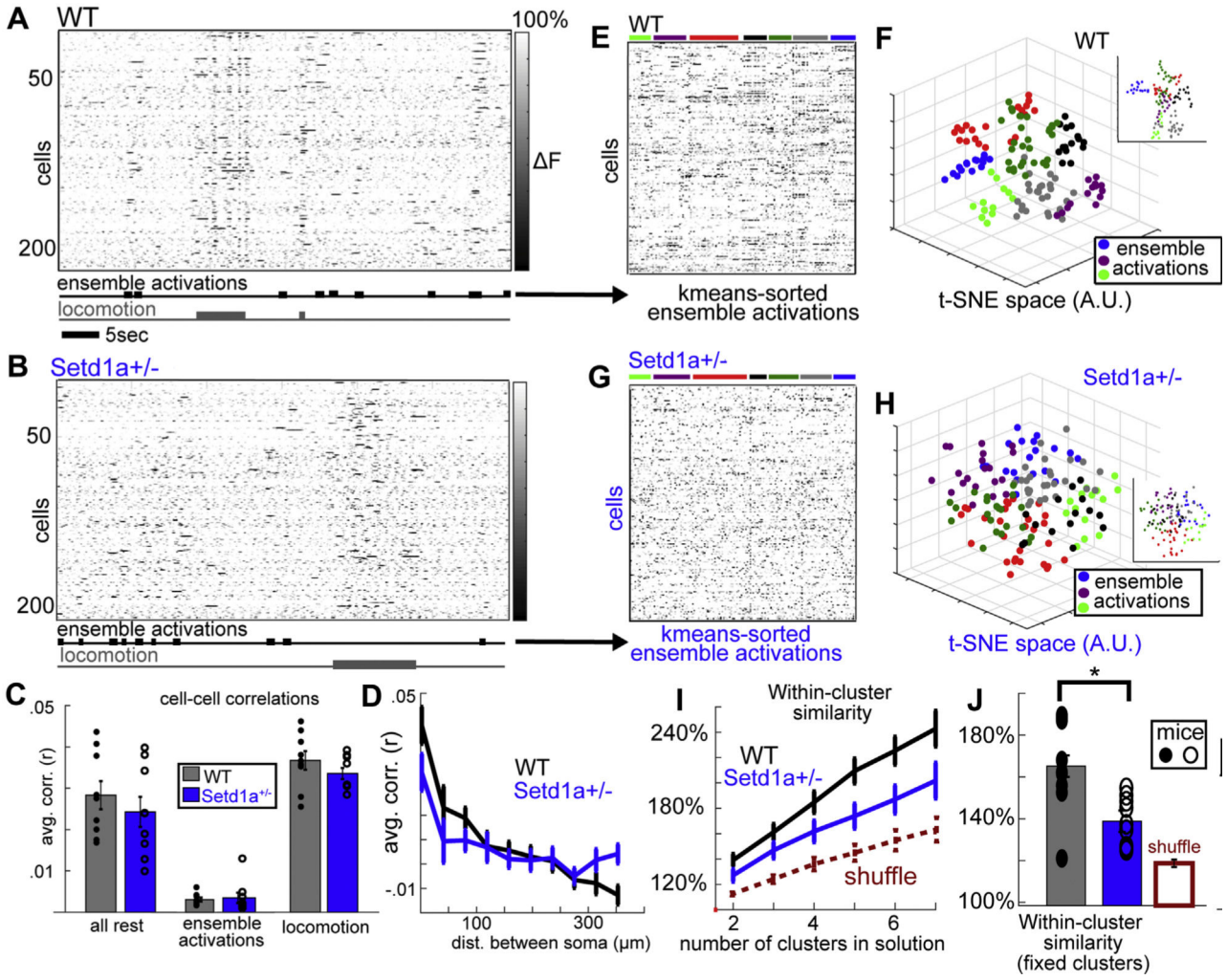

Figure 2.

Correlated activity and ensemble activations are altered in *Setd1a*$^{+/-}$ mice during ongoing activity. **(A, B)** Raster plots show multineuronal activity patterns present during ensemble activations (i.e., multiple coactive neurons in 1 frame) and locomotion periods from example **(A)** WT and **(B)** *Setd1a*$^{+/-}$ mice. **(C)** Overall correlations between cell pairs were not altered when cells were considered en masse, but **(D)** while WT mice showed a clear spatial gradient of spontaneous correlated activity, this effect was attenuated in *Setd1a*$^{+/-}$. **(E, F)** Sorting ensemble activation periods in WT mice with k-means clustering analysis (after *t*-SNE factorization) revealed multiple distinct reliable activity patterns. **(G, H)** This sorting procedure failed to identify such repeating patterns in *Setd1a*$^{+/-}$ mice. **(I)** This effect was quantified by comparing within-cluster vs. overall state-state similarity (i.e., spatial correlation of activity patterns) across increasing "k" values (numbers of clusters in fitted solution; $t_{13}^{\text{interaction}} = 2.5$, $p < .05$), as well as **(J)** when clusters were fixed to a function of the total cells recorded (i.e., 3 clusters per 100 cells; $t_{13} = 3.1$, $p < .01$). Both groups showed evidence of some structure compared with equivalent analyses of time-shuffled surrogate data [100 times per mouse; red dashed line in **(I)** and red-outlined bar in **(J)**]. The same effects held true when analyses were applied to visual stimulation periods (data not shown).

A.U., arbitrary units; dist., distance; *t*-SNE, *t*-distributed stochastic neighbor embedding; WT, wild-type.

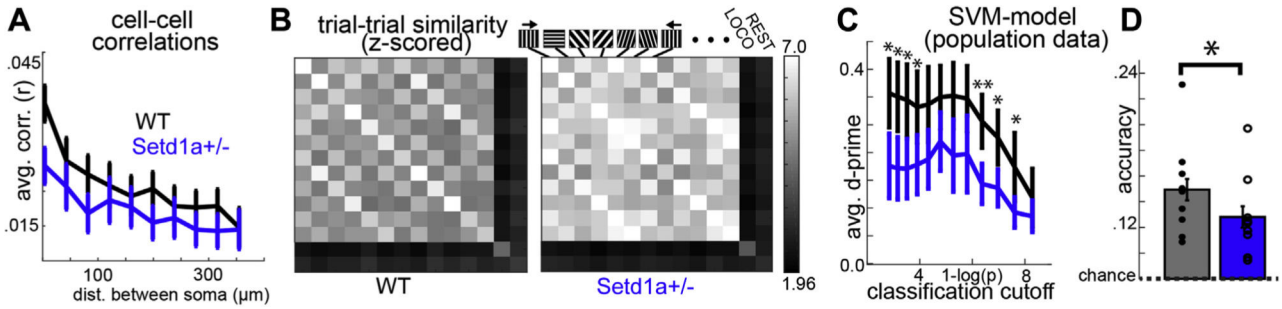

Figure 3.

Disrupted ensembles in visually evoked activity in *Setd1a*$^{+/-}$ mice. **(A)** Altered spatial distributions of cell-cell correlations during visual stimulation. **(B)** Matrices reflecting activity pattern similarities across trial types, locomotion, and rest, indicating distinct and shared population activities in response to different stimuli and states in WT and *Setd1a*$^{+/-}$mice. **(C)** Support vector machine algorithms were used to build linear classifiers for each stimulus on multineuronal data fitted on the first 5 trials. Models were applied to data collected on the last 5 trials and showed **(C)** reduced d-prime estimates (averaged over all stimulus type classifiers) and **(D)** reduced accuracy (best estimate across all classifiers) in *Setd1a*$^{+/-}$ mice (*t* tests: *$p < .05$, **$p > .01$; d-prime and accuracy were identical for WT and *Setd1a*$^{+/-}$ mice for the fitted models). dist., distance; loco, locomotion; WT, wild-type.

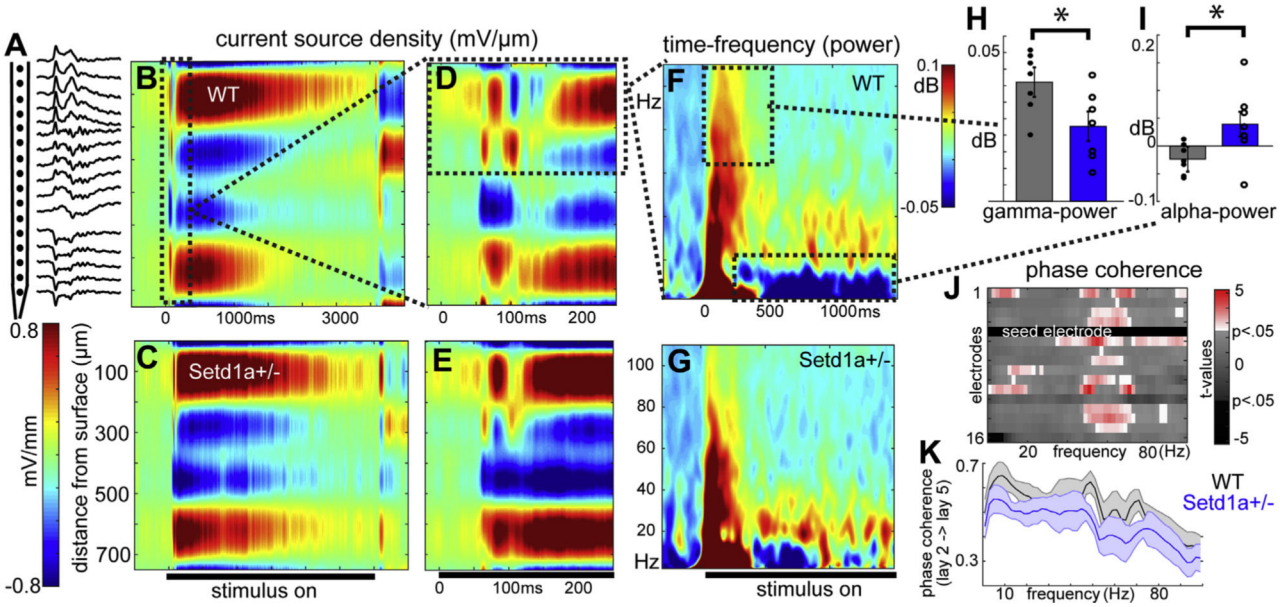

Figure 4.

Altered cortical oscillations in *Setd1a*$^{+/-}$ resembling sensory-processing biomarkers of schizophrenia. **(A)** Multielectrode local field potential recordings (16 channels) during visual stimulation **(B, C)** were analyzed as current source density estimates (2 example mice). **(D, E)** Same as **(B, C)** but zoomed in to show early stimulus-evoked currents. **(F, G)** Time-frequency decomposition with Morlet wavelets indicates **(H)** decreased stimulus-evoked high-frequency oscillations and **(I)** altered alpha-band desynchronization [similar to electroencephalography studies in human schizophrenia (54,55)]. **(J)** Results from *t* tests comparing values of within-trial phase coherence between 1 electrode in putative layer 2/3 and other contacts across all frequencies (subtracting trial-shuffled surrogate) reveals a pattern of altered alpha- and gamma-phase coherence across the cortical column. **(K)** Single comparison of layer 2/3 vs. layer 5 coherence [electrodes 5 and 11 from **(J)**, with actual phase coherence values, *R* statistic]. **t* test: $p < .05$. WT, wild-type.

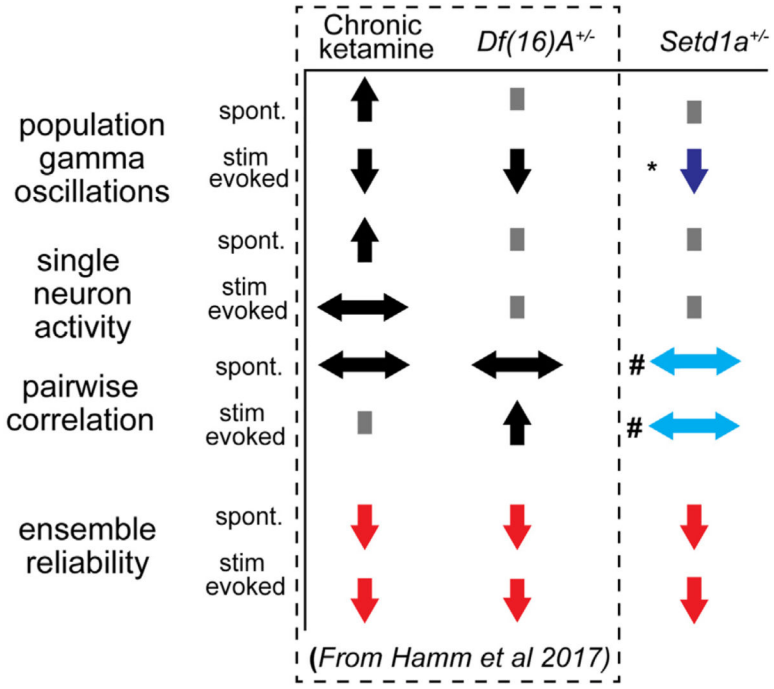

Figure 5.

Summary of effects and comparison with other models of schizophrenia pathophysiology/risk. Local field potential, cellwise, pairwise, and ensemblewise effects are summarized with up-arrows signifying an increase, down-arrows a decrease, left/right arrows a change in distribution, and squares no change. Deficits are the most consistent across models and conditions at the level of ensemble function. *Stimulus-evoked changes in gamma in *Setd1a* $^{+/-}$ mice affected high-gamma rather than low/mid-gamma as seen in other models. #Changes in pairwise correlations were spatial in *Setd1a*$^{+/-}$ mice, not distributional. Distributional changes were not observed in *Setd1a*$^{+/-}$ mice. spont., spontaneous. [Adapted from Hamm *et al.* (14).]